ACS NANO

www.acsnano.org

ARTICLE

# Magnetic Phases and Zone-Folded Phonons in a Frustrated van der Waals Magnet

Amit Pawbake,[○] Florian Petot,[○] Florian Le Mardelé, Tristan Riccardi, Julien Lévêque, Benjamin A. Piot, Milan Orlita, Johann Coraux, Michal Hubert, Jan Dzian, Martin Veis, Yurii Skourski, Bing Wu, Zdenek Sofer, Benoît Grémaud, Andrés Saúl,* and Clément Faugeras*

Cite This: *ACS Nano* 2025, 19, 23693−23702

Read Online

ACCESS | Metrics & More | Article Recommendations | Supporting Information

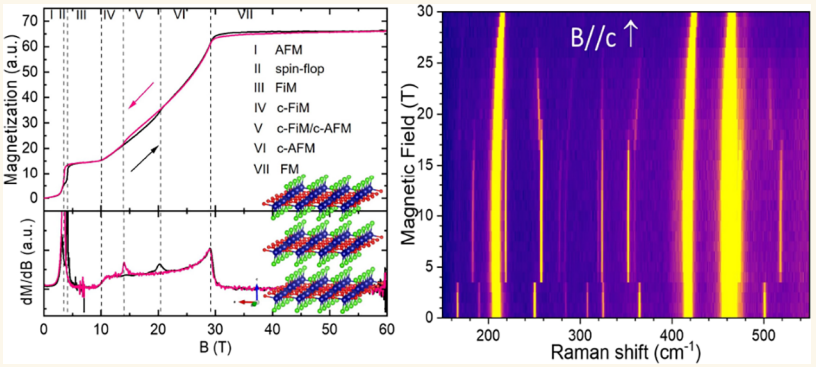


**ABSTRACT:** **2D magnetic materials have attracted extensive research interest due to their potential application in nanospintronics, optospintronics, and magnonics. Ferromagnetic- and antiferromagnetic-layered materials have been demonstrated and successfully inserted into van der Waals heterostructures. However, the effects of magnetic frustration in van der Waals materials and the possibilities offered by spin configurations characterized by nonlinear spin arrangements have not been fully considered yet. Herein, we establish the magnetic phase diagram of bulk CrOCl, a frustrated van der Waals magnet, using magnetization and magneto-optical spectroscopy techniques. In particular, we use the magnetic superstructures relative to the crystallographic unit cell and the associated rich zone-folded phonon series to describe the magnetic-field-induced phases. Theoretical calculations taking into account the competing nearest neighbors' magnetic exchange interactions provide insight into the lattice vibrations of this class of magnetic system. This study expands the scope of 2D magnetic materials and provides a methodology to characterize frustrated van der Waals magnets.**

**KEYWORDS:** *van der Waals magnet, Raman scattering, zone-folded phonons, density functional theory, magnetic phases*

Downloaded via CNRS REGION RHONE ALPES on July 9, 2025 at 08:15:35 (UTC).
See https://pubs.acs.org/sharingguidelines for options on how to legitimately share published articles.

## INTRODUCTION

On-lattice frustration, in certain magnetic compounds featuring spin−spin interactions of various kinds between first, second, and neighboring lattice sites, leads to very rich magnetic phase diagrams comprising highly degenerate disordered phases and complex spin orders. Varying the temperature, magnetic field, or hydrostatic pressure, one can navigate through these exotic phase diagrams. Spectacular examples of emerging exotic quantum phases[1,2] and cascades of magnetic ground states driven by an external magnetic field[3−7] or hydrostatic pressure[8,9] have been reported in the last years.

van der Waals magnetic materials are layered materials that can be thinned down to the monolayer limit, while retaining collective magnetic properties,[10] different in nature from those of the bulk parent material.[11] They altogether offer a broad portfolio of intralayer magnetic ordered states, such as ferromagnetism (FM), Néel-like zigzag, or stripe antiferromagnetism[10,12,13] (AFM), combined with ferro- or antiferromagnetic interlayer interactions.[14] Accordingly, they represent a rich platform to revisit and further explore low-dimensional magnetism, with new opportunities as they can be inserted within van der Waals heterostructures[15] to induce specific

Received: February 21, 2025
Revised: June 11, 2025
Accepted: June 13, 2025
Published: June 23, 2025

ACS Publications

© 2025 The Authors. Published by American Chemical Society

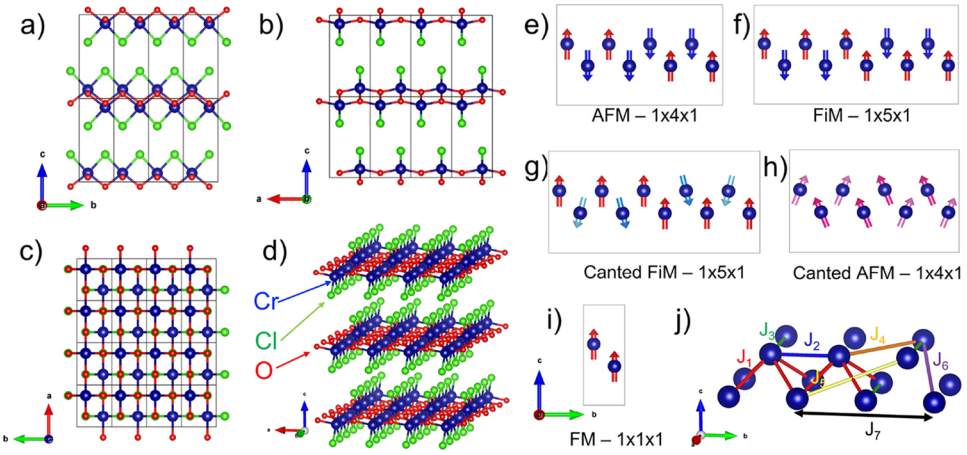


**Figure 1. (a–c) Crystal structure of bulk CrOCl along the main crystallographic axes and (d) perspective view of the lattice. The field-induced magnetic phases of CrOCl considered in this work: (e) Antiferromagnetic (AFM) with a $4\vec{b}$ period; (f) ferrimagnetic (FiM) with a $5\vec{b}$ period compatible with a 1/5 total magnetization; (g) canted FiM phase with a $5\vec{b}$ period; (h) canted AFM phase with a $4\vec{b}$ period; (i) ferromagnetic (FM); and (j) definition of the Cr–Cr magnetic exchange parameters $J_i$.**

properties in the neighboring layers via proximity effects;[16−18] they may even pave the way to an ultimately thin (van der Waals) spintronics.[19]

Depending on the lattice structure and on the nature/strength of spin–spin interactions between different kinds of neighbor sites, these interactions may have antagonistic effects, each promoting alone a different kind of order. Such competition of interactions prevents simple (i.e., ferro or antiferromagnetic) spin orders to develop and instead favors nontrivial spin arrangements. Bulk chromium oxychloride CrOCl falls in this class of compounds—it is a frustrated magnet, possessing a rich phase diagram, whose phases have only been partly assigned.

At room temperature, CrOCl crystallizes in the orthorhombic FeOCl structure with the *Pmmn* space group[20,21] (see Table S1 of the Supporting Information). The crystal structure of CrOCl, together with the relevant views along the $\vec{a}$, $\vec{b}$, and $\vec{c}$ axes, is presented in Figure 1a–d. When decreasing temperature, magnetic correlations become significant below 27 K, where an incommensurate spin density wave builds up,[22] which then evolves below the Néel temperature $T_N$ = 14 K into an antiferromagnetic (AFM) state with a $4\vec{b}$ period[21] (see Figure 1e). Even though the size of the magnetic unit cell is $4\vec{b}$, X-ray experiments detected a $2\vec{b}$ structural distortion,[23] accompanied by a distortion to a monoclinic lattice with the $P2_1/m$ space group.

The $4\vec{b}$ periodicity of the magnetic order is a consequence of the frustration in the magnetic exchange parameters, as defined in Figure 1j. Exchange interactions calculated using density functional theory (DFT) methods and the broken symmetry formalism,[24−29] i.e., by mapping total energies corresponding to various collinear spin arrangements within a supercell onto the Heisenberg Hamiltonian, are presented in the S3 of the Supporting Information. The leading exchange interactions are $J_1$, $J_2$, $J_3$, and $J_7$. As can be seen in Figure 1j, FM interaction $J_3$ connects Cr atoms in different unit cells along the *a* axis and does not lead to a new periodicity along this direction. Frustration is due to incompatible interactions between $J_1$ (AFM), $J_2$ (FM), and $J_7$ (AFM). In particular, $J_7$ is mainly responsible for stabilizing the four times periodicity along the $\vec{b}$ axis.

When a magnetic field is applied along the $\vec{c}$ axis, bulk CrOCl undergoes a series of magnetic phase transitions first to a spin-flop phase around $B$ = 3.0 T and then to a ferrimagnetic (FiM) phase (see Figure 1f) above $B$ = 3.85 T. This phase has been inferred from the observation of a plateau in the magnetization[30] corresponding to 1/5 of the magnetization at saturation. For $B$ > 4 T, an apparent splitting of a phonon with $A_g$ symmetry[30] has been assigned to a Raman scattering signature of the FiM phase. Above the FiM state, the high-magnetic-field phases of CrOCl are not known even though it has been shown that the magnetic lattice saturates at $B$ = 30 T.[22] Recently, thin layers of CrOCl down to the monolayer have been investigated by magneto-tunneling measurements,[31] suggesting magnetocrystalline anisotropies more subtle than the easy-axis anisotropy for bulk CrOCl.[31,32]

In this work, we present magneto-Raman scattering and magneto-infrared (IR) absorption spectroscopy analysis of phonon modes in bulk CrOCl, confronted with magnetization versus magnetic field measurements up to high magnetic fields (30 T continuous, 60 T pulsed) and DFT calculations. Our results show that the magnetic frustration in this van der Waals magnet induces magnetic phases with unit cells much larger than the crystallographic one. This additional magnetic periodicity changes both the phonon Raman scattering and the infrared responses by folding the phonon Brillouin zone onto the Γ point. We observe a series of zone-folded phonons (ZFPs) in the low-temperature AFM phase, which changes under an external magnetic field into another series of ZFP modes in the FiM phase and which persists up to $B$ = 19 T. Above this magnetic field, the series of ZFP modes transforms again into another series of ZFP similar to that observed at $B$ = 0, indicating, at high magnetic fields, the presence of a magnetic phase with the same periodicity as the AFM phase. For $B$ > 19 T, all Raman-active phonons experience a gradual change of their energies, as large as 1 meV, up to the saturation magnetic field of $B$ = 30 T. In particular, the ZFP modes allow for spectroscopy of the magnetic ground states and also reflect the magnetic hysteresis as observed when sweeping the magnetic field in opposite directions.


https://doi.org/10.1021/acsnano.5c03174
ACS Nano 2025, 19, 23693−23702

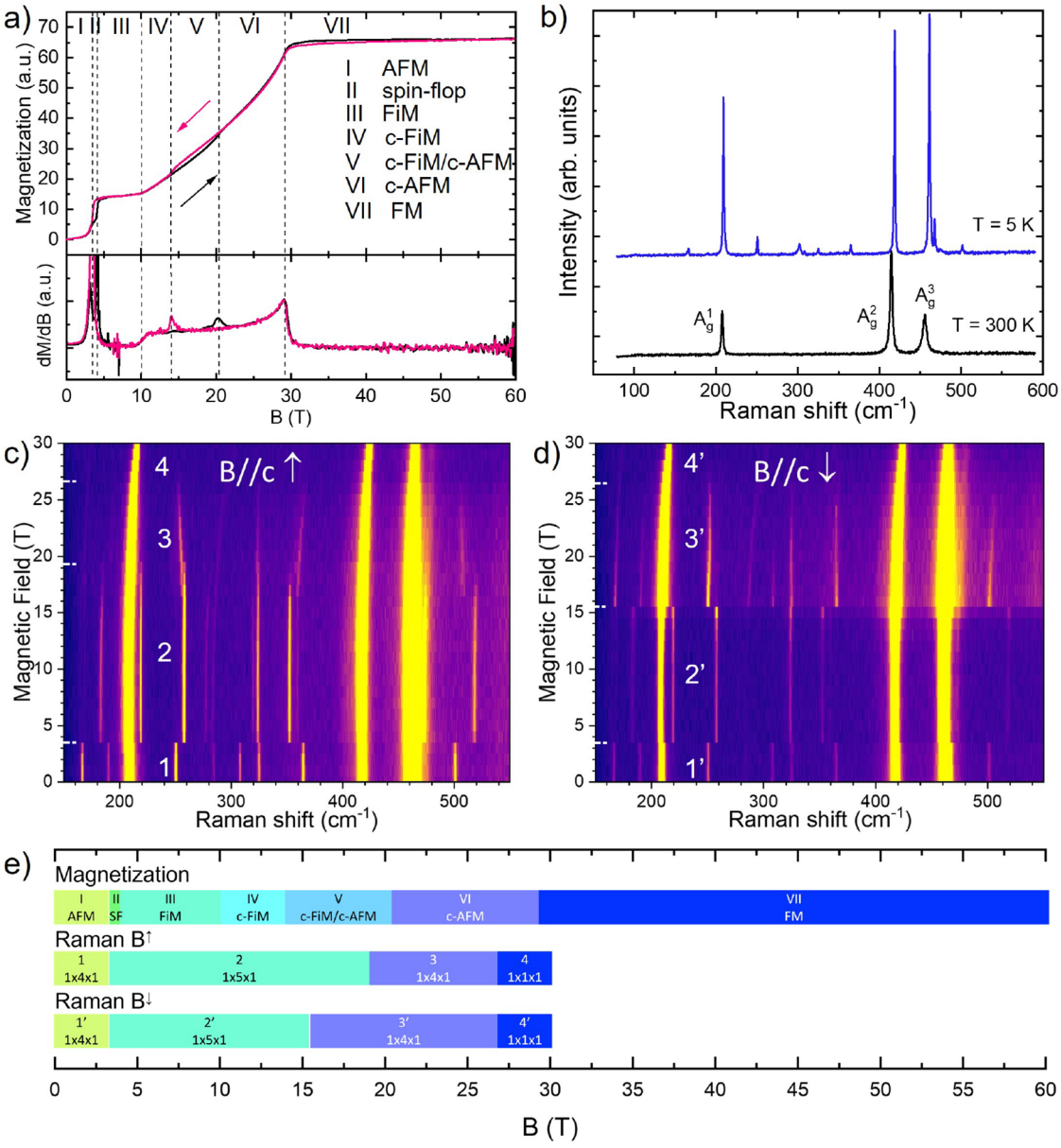


**Figure 2. (a) Low-temperature (4.5 K) magnetization curve of bulk CrOCl with the magnetic field applied along $\vec{c}$. The data for $B < 7$ T have been measured with SQUID magnetometry, and in pulsed magnetic fields for $B > 7$ T, see Figure S8 of the Supporting Information. Vertical dashed lines indicate the critical magnetic fields separating the different magnetic regions labeled by Roman numbers. (b) Raman scattering response of bulk CrOCl measured at room temperature and at $T = 5$ K. (c,d) Magneto-Raman scattering spectra acquired when sweeping the magnetic field along $\vec{c}$ (c) from 0 to 30 T and (d) from 30 T to 0 measured with 1 T field increments/decrements. Four different regions can be defined when sweeping the magnetic field up or down, labeled with Arabic and primed Arabic labels, respectively (see text). (e) Schematic comparison of the different regions associated with specific behaviors in the magnetization versus magnetic field measurements and the Raman scattering response when sweeping the magnetic field up and down, as shown in panels a, c, and d.**

Using DFT calculations, we describe the phonon modes of different ground states. The theoretical calculations of the ZFP modes compare well with the experimental observations, supporting the presence of magnetic phases with unit cells much larger than the crystallographic one. Using an *unfolding* procedure,[33] we were able to assign the series of ZFP to the $\vec{k} \neq \vec{0}$ phonon modes of the crystallographic cell.

Finally, experiments performed with the external magnetic field applied along the in-plane directions show that bulk CrOCl has not only an easy magnetic axis along $\vec{c}$ but also an intermediate and a hard axis in the plane of the layers.

## MAGNETIZATION MEASUREMENTS

Figure 2a shows the magnetization (M) as a function of a magnetic field applied along the $\vec{c}$ axis, measured up to $B = 60$ T. Seven different regions can be defined in the $M$ vs $B$ plot. They have been labeled with Roman numerals in Figure 2a. As mentioned above, the zero field phase, region I in Figure 2a, is an AFM phase (see Figure 1e) with a $4\vec{b}$ period,[21] which is maintained up to $B \sim 3.5$ T, in our experiment performed at 4.5 K.[22,23,30,31,34] Magnetization increases linearly as a function of the B field in this phase. We understand this behavior as possibly originating from the finite temperature at which the



https://doi.org/10.1021/acsnano.5c03174
ACS Nano 2025, 19, 23693−23702

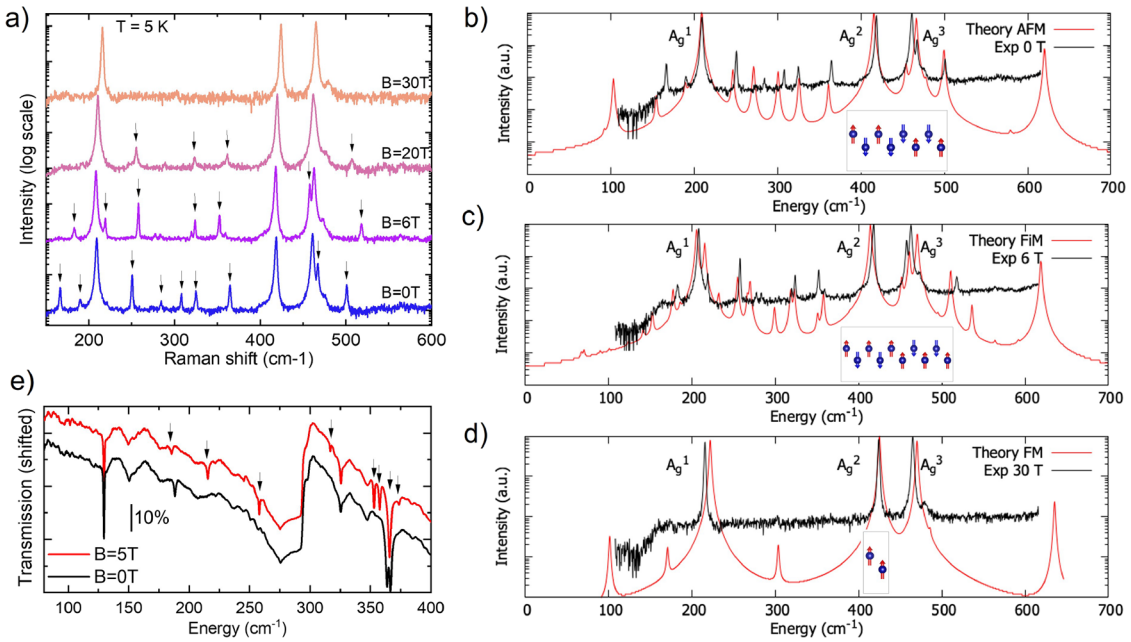


**Figure 3. (a) Low-temperature Raman scattering response of bulk CrOCl at selected values of the magnetic field applied along $\vec{c}$ and corresponding to the AFM, to the FiM, the canted antiferromagnetic, and to the FM phases (log scale). Arrows indicate the zone-folded phonons. (b–d) Experimental spectra (5 K) compared to theoretical calculations (log. scale; theoretical energies stretched by 6%, structures used for calculation have been fully relaxed); (b) measurement at 0 T, calculation for an AFM 1 × 4 × 1 monoclinic unit cell; (c) measurement at 6 T, calculation for a FiM 1 × 5 × 1 orthorhombic unit cell; (d) measurement at 30 T, calculation for a FM 1 × 1 × 1 orthorhombic unit cell; (e) low-temperature IR transmission spectra measured at $B$ = 0 T (AFM phase) and at $B$ = 5 T (FiM phase). Arrows indicate the zone-folded phonons.**

experiment is performed and potential paramagnetic impurities in our bulk specimen.

A first hysteresis cycle is observed between 3.5 and 4 T (region II in Figure 2a). When increasing the magnetic field in this region (black curve), the small plateau at around one tenth of the saturation magnetization has recently been assigned to the transition from the low-temperature AFM state to a spin-flop phase, which then evolves to a FiM state characterized by a magnetization plateau (region III) at one-fifth of the magnetization.[30−32,35] The proposed magnetic order for the FiM phase in the 10-spins unit cell is depicted in Figure 1f, with 6 spins (respectively 4) aligned (respectively, antialigned) with the field direction.[30,31] It is interesting to note that this magnetic order with a $5\vec{b}$ periodicity is the simplest conceivable one with 1/5 of the total magnetization; however, other orders might be relevant. The magnetization plateau associated with the ferrimagnetic phase extends up to $B$ = 10 T.

We have performed magneto-optical Kerr effect experiments that show the appearance of a net magnetization in CrOCl above $B$ = 4 T; see Figure S9 of the Supporting Information. The field-dependent Kerr rotation spectra exhibit a sudden increase in amplitude above 3.5 T when a spectroscopic structure around 1.7 eV appears. This corresponds to the Kerr rotation originating from interband transitions across the band gap in the ferrimagnetic phase. The ferrimagnetic origin of the polar Kerr rotation is proven by its sign change upon the change of the sign of the external magnetic field and a relative saturation between 4.5 and 6 T. Above 10 T (regions IV, V, and VI in Figure 2a), the magnetic phases have not been identified so far. Based on our Raman scattering experiments and DFT calculations, we provide new insights into the magnetic order associated with them (see below). Around $B$ = 29 T, magnetization saturates and remains constant (region VII) up to the highest value of the magnetic field accessible in our experiment, $B$ = 60 T. CrOCl is then fully polarized in an FM state (see cartoon in Figure 1i).

Evaluating the magnetic susceptibility d$M$/d$B$, see the lower panel of Figure 2a, we can identify two anomalies: at $B$ = 20.5 T when sweeping the magnetic field up and at $B$ = 14 T when sweeping down. We understand these peaks in the susceptibility as signatures of magnetic phase transitions, which imply that sweeping the magnetic field up, the canted FiM phase extends up to $B$ = 20.5 T, and that when sweeping the B field down, the canted AFM phase extends down to $B$ = 14 T. This magnetization curve will serve as a guide to interpret the results of Raman scattering and infrared spectroscopy experiments.

## RAMAN SCATTERING MEASUREMENTS

**Temperature Dependence.** The Raman scattering response of bulk CrOCl at 5 and 300 K is presented in Figure 2b. At room temperature, it is composed of three contributions identified as phonons with $A_g$ symmetry[34] and labeled $A_g^{1-3}$. They correspond to atomic displacements along the $\vec{c}$ axis (see Figure S11 of the Supporting Information). The other six Raman-active modes with $B_{2g}$ and $B_{3g}$ symmetries and displacements along the $\vec{a}$ and $\vec{b}$ axes are expected to have extremely low intensities and cannot be observed in our experiment.

When decreasing temperature, on top of these prominent phonon modes (hardened under the effect of anharmonicity), another series of Raman scattering features with much lower intensity can be seen clearly at 5 K; see Figure 2b. The full


https://doi.org/10.1021/acsnano.5c03174
ACS Nano 2025, 19, 23693−23702

temperature dependence can be found in Figures S1 and S2 of the Supporting Information. These modes become optically active when the long-range magnetic order is settled and a magnetic unit cell, with a different size than the crystallographic cell, appears. This is the case when the AFM ground state with a $4\vec{b}$ periodicity is stabilized below $T_N$ = 14 K. Figure 3b shows the comparison of the experimental Raman spectra at zero field and 5 K and the DFT calculations for the fully relaxed 1 × 4 × 1 monoclinic unit cell with the AFM magnetic order shown in Figure 1e. The calculated parameters of the relaxed AFM cell are presented in Table S2 of the Supporting Information. The calculation confirms that the low-intensity Raman features arise from two effects: the change in symmetry, from orthorhombic to monoclinic, and the magnetoelastic distortions induced by the magnetic order; see Figures S9 and S10 of the Supporting Information.

It is important to note here that the spin superperiodicity developed below $T_N$ does not explain, alone, the appearance of folded phonon modes in the Raman spectra because the electromagnetic wave does not interact with the spin but with the full charge density. As is the case in CrOCl, most magnetic phase transitions are accompanied by small lattice distortions producing a superperiodicity (relative to the nonmagnetic crystal periodicity). The Raman activity of such modes depends on the amplitude of the lattice distortion, which is traced back to the strength of the magneto-elastic interaction. The additional features in the spectra thus reflect the different magnetic phases through the lattice distortion mentioned above and can be used to reveal the field-induced magnetic phases.

**Magnetic Field Dependence.** The magnetic field dependence of the Raman scattering response for increasing fields is shown in Figure 2c, and in Figure 3a for 0, 6, 20, and 30 T.

When increasing the magnetic field, the series of additional features characteristic of the AFM 1 × 4 × 1 phase changes abruptly (within 100 mT) to another series for $B$ > 3.85 T (see Figure S3 in the Supporting Information). This observation indicates that at this particular magnetic field, small displacements of the atomic positions occur following a change in the magnetic ground state and in the size of the magnetic unit cell. This is consistent with our understanding of the periodicity of the magnetic phases of bulk CrOCl that change from $4\vec{b}$ in the AFM phase to $5\vec{b}$ in the FiM phase. Good agreement is found between the series of low-intensity Raman-active modes of the FiM phase measured at 6 T and the DFT calculations for the fully relaxed 1 × 5 × 1 orthorhombic cell with the FiM magnetic order (Figure 1f), as seen in Figure 3c. The calculated parameters of the relaxed FiM cell are presented in Table S3 of the Supporting Information.

Increasing further the magnetic field, this series of low intensity features persists up to 19 T, where it abruptly changes to another series, which is strongly reminiscent of the one observed at 0 T. Comparing the position of the peaks marked with arrows in the Raman scattering response for 0 and 20 T in Figure 3a, all the peaks present at 20 T appear to be slightly hardened versions of the modes at 0 T (some of the low-intensity features are only visible at 0 T). This series persists up to 27 T and then progressively vanishes. From 27 T up to 30 T, the Raman scattering response is only composed of the three high-intensity $A_g$ phonon peaks of the FM phase. We observe a blue shift of the three $A_g$ modes at 30 T with respect to those at 20 T. The full magnetic field dependence showing a $B^2$ hardening of their energies is presented in Figure S5 of the Supporting Information. The comparison of the experimental Raman scattering response at 30 T to the DFT-calculated spectra for the 1 × 1 × 1 orthorhombic cell with the FM magnetic order shown in Figure 1i is presented in Figure 3d. The calculated parameters of the relaxed FM cell are presented in Table S4 of the Supporting Information.

The additional features also show magnetic hysteresis. As shown in Figure 2d, when sweeping down the magnetic field after having reached the magnetization saturation at $B$ = 30 T, the magnetic field values at which the series changes are different. From Figure 2c,d, we can thus identify four different regions in the magneto-Raman scattering response of bulk CrOCl, which we have labeled with Arabic and primed Arabic labels, from 1 to 4 and 1′ to 4′, respectively. The main difference between increasing and decreasing the magnetic field concerns the critical field that defines the transition between regions 2 and 3 (19 T), to be compared to the transition between 2′ and 3′ (15.5 T). A series of additional Raman-active modes can hence be used as a tool to evaluate and characterize magnetic hysteresis.

Such additional features are also observed with different selection rules when measuring the infrared (IR) transmission of bulk CrOCl. The low-temperature IR transmission spectra measured at $B$ = 0 T (AFM phase) and at $B$ = 5 T (FiM phase) are presented in Figure 3e. They present distinct sharp absorption features that correspond to additional IR-active modes, distinct from the Raman-active series, and the series abruptly changes to another series at the magnetic phase transition. They offer deeper insight into the phonon band structure as they provide the IR-active modes. The magnetic evolution of the IR response up to $B$ = 16 T is presented in Figures S6 and S7 of the Supporting Information.

The comparison between the seven magnetic field regions defined from the magnetization versus magnetic field measurements (labeled with Roman numbers) and the ones defined from the Raman scattering measurements is shown in Figure 2e. From this, we discuss the nature of the magnetic phases associated with the regions labeled IV, V, and VI in Figure 2a,e. The increase in magnetization in the 10−14 T range (region IV) is certainly a canted phase with the same periodicity ($5\vec{b}$) as the FiM phase. Its magnetic order is represented schematically in Figure 1g. The increase in magnetization in the 20.5−30 T range (region VI) must be a canted phase with the periodicity ($4\vec{b}$) of the AFM phase. The magnetic order of this canted AFM phase is schematically represented in Figure 1h. The hysteresis cycle in the 14−20.5 T range (region V) corresponds to a competition between these two canted phases. At this stage, the spin-flop phase detected in the magnetization measurements in the 3−3.85 T range (region II in Figure 2a) cannot be distinguished from the AFM 1 × 4 × 1 phase as both phases share the same (magnetic) periodicity.

## ZONE-FOLDED PHONONS

The additional Raman and infrared active modes that appear at a low temperature and under a magnetic field can be, in general, attributed to small distortions that change the crystallographic symmetry of the unit cell. In bulk CrOCl, the paramagnetic and the FM phases have the same orthorhombic structure with the *Pmmn* space group. The


https://doi.org/10.1021/acsnano.5c03174
ACS Nano 2025, 19, 23693−23702

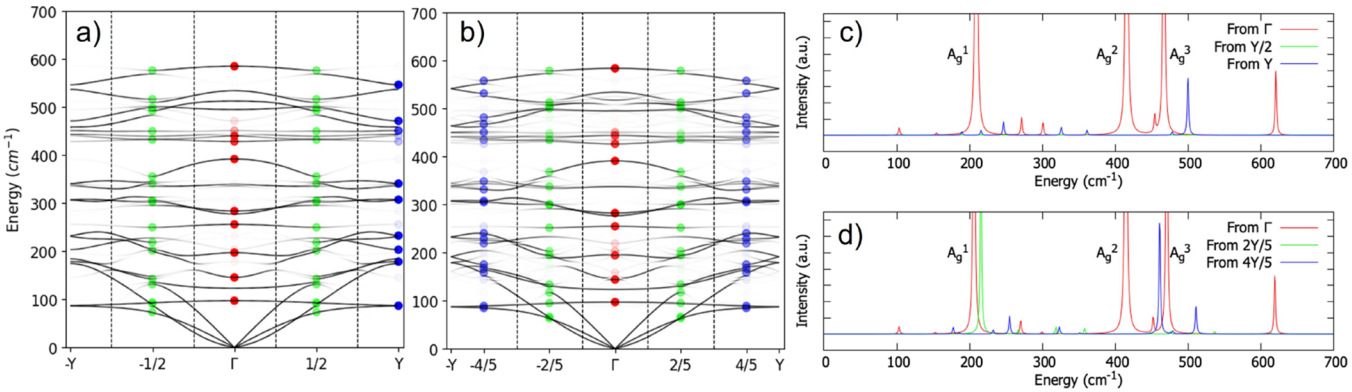


**Figure 4. (a) Calculated phonon band structure of the fully relaxed 1 × 4 × 1 AFM phase unfolded in the Brillouin zone of the 1 × 1 × 1 unit cell. The gray hue of the lines represents the weight in the unfolding procedure (see the text). The dots at Γ (red), ± $Y/2$ (green), and $Y$ (blue) are the 36 Raman-active modes of the 1 × 4 × 1 AFM phase unfolded in the 1 × 1 × 1 Brillouin zone. (b) Similar unfolding process performed for the fully relaxed 1 × 5 × 1 FiM band structure. The dots at Γ (red), ± $2Y/5$ (green), and ± $4Y/5$ (blue) are the 45 Raman-active modes of the 1 × 5 × 1 FiM phase unfolded in the 1 × 1 × 1 Brillouin zone. (c) Calculated intensity of the 36 Raman-active modes shown in panel (a). (d) Calculated intensity of the 45 Raman-active modes shown in panel (b).**

AFM magnetic order is monoclinic with the $P2_1/m$ space group, and the FiM phase is orthorhombic with the *Pmmn* space group. As already mentioned, the AFM unit cell is four times larger along the $\vec{b}$ axis than the paramagnetic one, and the FiM unit cell is five times larger. One can thus wonder if the additional features appearing in the Raman scattering response could be understood as additional modes that appear at Γ as a result of the zone folding of the 1 × 1 × 1 cell. Indeed, from group theory analysis, there are nine Raman-active phonons in the paramagnetic or FM phase, 36 in the AFM phase, and 45 in the FiM phase.

The phonon band structure of the fully relaxed 1 × 1 × 1 FM cell is shown in Figure S12 of the Supporting Information. The result of folding this band structure four and five times smaller Brillouin zones is also shown. They are compared, side-by-side, with those of the corresponding fully relaxed AFM and FiM phonon bands. One can observe small energy differences and band anticrossings, which are a consequence of the small structural distortions produced by the magnetoelastic interactions. It is important to note that even if the phonons generated by the strict zone-folded process of the 1 × 1 × 1 cell will appear as Raman or IR active by the group theory analysis, their intensity will be zero. No new modes can appear by *unnecessarily* changing the size of the unit cell. It is the small displacement of the atomic positions due to the magnetoelastic interactions, evidenced by the slight change of their energies that make them visible.

The phonon band structure of the fully relaxed 1 × 4 × 1 AFM and 1 × 5 × 1 FiM magnetic systems (see Figure S12 of the Supporting Information) can be *unfolded* in the Brillouin zone of the 1 × 1 × 1 cell through the procedure proposed by Allen et al.[33] The $L$ phonon mode with wave vector $\vec{K}$ in the AFM (FiM) Brillouin zone and energy $\omega(\vec{K}L)$ will appear with a weight

$$W_{\vec{K}L}(\vec{G}) = \frac{1}{\mathcal{N}} \sum_{j=1}^{\mathcal{N}} \langle \vec{K}L|\hat{T}(\vec{r_j})|\vec{K}L\rangle e^{-i(\vec{K}+\vec{G})\cdot\vec{r_j}}$$

and the same energy at wave vector $\vec{G}$ in the Brillouin zone of the 1 × 1 × 1 cell. Here, $\mathcal{N}$ is the number of crystal unit cells in the magnetic supercell (4 for AFM and 5 for FiM), and $\hat{T}(\vec{r_j})$ is the translation operator of 1 × 1 × 1 unit cells labeled with index $j$ along the $\vec{b}$-axis. The resulting phonon band structures for the AFM and FiM systems are shown in Figure 4a,b, where the hue of the gray lines represents the weight of the unfolding procedure. There is a strong resemblance between the unfolded phonon band structures with the band structure of the 1 × 1 × 1 cell shown in Figure S12 of the Supporting Information. The 36 red, green, and blue dots in Figure 4a and 45 in Figure 4b are the Raman-active modes with $\vec{K} = \Gamma$ unfolded in the Brillouin zone of the 1 × 1 × 1 cell. As expected, the ZFP of the AFM cell comes from Γ (red), ± $Y/2$ (green), and $Y$ (blue) in the 1 × 1 × 1 cell and the ZFP of the FiM cell comes from Γ (red), ± $2Y/5$ (green), and ± $4Y/5$ (blue).

This unfolding procedure allows us to identify the origin of the additional features that appear in the Raman response and assign them to the points of the 1 × 1 × 1 Brillouin zone commensurate with the magnetic periodicity. The result is shown in Figure 4c,d, where the calculated Raman spectra are plotted with the same colors as in the unfolded band structure. Additional features in the FiM spectra can be assigned to ZFP from $\vec{G} = \Gamma$, $2Y/5$, and $4Y/5$. We can see that the apparent splitting of the $A_g^1$ and $A_g^3$ recently reported[30] for the FiM phase is actually the result of the appearance of ZFP from $2Y/5$ and $4Y/5$, respectively.

For the AFM phase, only ZFP from $\vec{G} = \Gamma$ and $Y$ appear as new features in the Raman spectra. The intensity of ZFP from $\vec{G} = Y/2$ is strictly zero. This effect has its origin in the fact that ZFP from $Y/2$ are expected for a $4\vec{b}$ periodicity, such as in the AFM phase; however, as already mentioned, the structural distortion of this phase has only a $2\vec{b}$ periodicity. This result is confirmed by our calculations of the magnetic order of the AFM phase (see Figure S9 of the Supporting Information). The spin configurations presented in Figure 1e–i are schematics and correspond to the simplest ones compatible with the size of the magnet unit cells deduced from Raman scattering measurements. There could be additional interactions leading to noncollinear spin arrange-


https://doi.org/10.1021/acsnano.5c03174
ACS Nano 2025, 19, 23693–23702

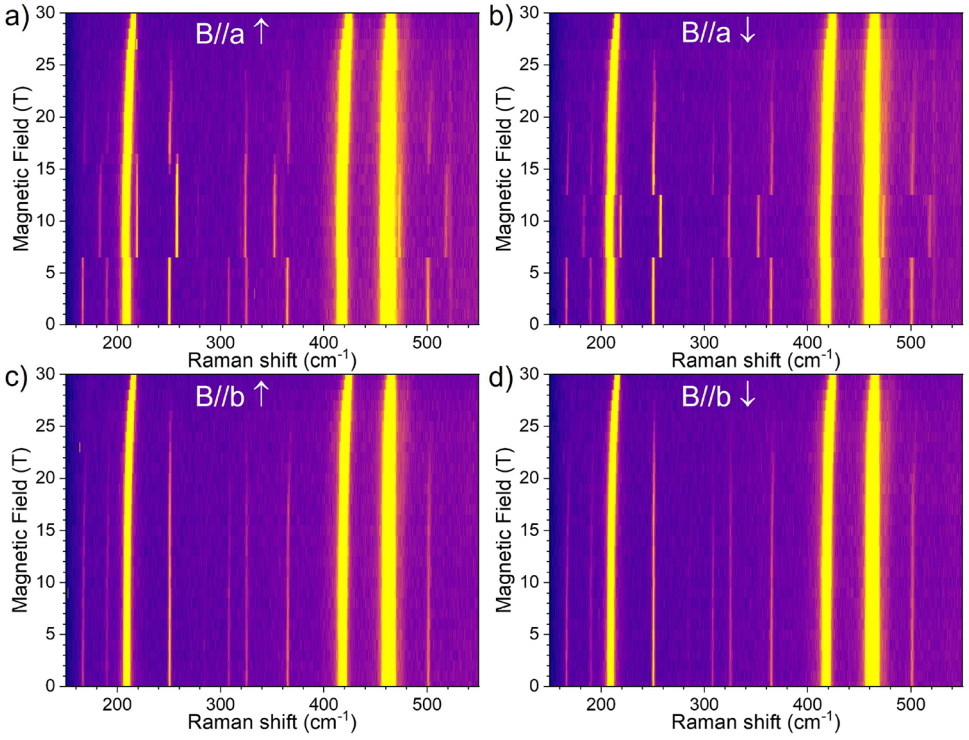


**Figure 5. False color map of the low-temperature magneto-Raman scattering response of bulk CrOCl with the *B* field applied along the long axis of the needles and sweeping from *B* = 0 to 30 T (a) and from *B* = 30 T to 0 (b) and with the magnetic field applied along the short axis of the needle while sweeping from *B* = 0 to 30 T (c) and from *B* = 30 T to 0 (d). The spectra are measured with a 1 T field increment/decrement.**

ments, such as hidden Dzyaloshinskii–Moriya interactions,[36,37] which are not taken into account in the present work.

## MAGNETOCRYSTALLINE ANISOTROPY

Having established previously that one can trace various magnetic phase transitions using ZFP spectroscopy when the B field is applied along the $\vec{c}$ axis, we now consider a magnetic field along the in-plane $\vec{a}$ and $\vec{b}$ directions. Exfoliation of bulk CrOCl produces lamellar needles with a long ($\vec{a}$ axis) and short axis ($\vec{b}$ axis), similar to the case of CrSBr.[38] Applying the field along $\vec{a}$, the *B*-sequence of ZFP spectra essentially changes by the values of the critical fields separating the FiM and the canted FiM phases (regions 1 and 2 or 1′ and 2′ in the Raman response in Figure 2) and separating the canted FiM and the canted AFM phases (regions 2 and 3 or 2′ and 3′ in Figure 2). The critical fields are 6.5 and 15.5 T upon increasing the field, instead of 3.5 and 19 T (compare Figures 2c and 5a). When the B field is swept from 30 T down to 0, a hysteresis is also observed with critical fields observed at 12.5 and 6.5 T, again different from the case of a field applied along $\vec{c}$ (compare Figures 2d and 5b). When the field is applied along the short axis of the needle, the observed evolution is distinct, with no change of the ZFP series up to the highest value of the magnetic field (see Figure 5c,d), suggesting that the FiM phase cannot be stabilized in this configuration. For both in-plane field orientations, the magnetoelastic interaction starts to be effective and shifts the three main phonon modes above 25 T. These experiments set bulk CrOCl in the class of biaxial magnetic systems.

## CONCLUSIONS

This study establishes CrOCl as a frustrated van der Waals magnet, with a rich phase diagram governed by competing magnetic interactions. Using magnetometry, magneto-Raman, and infrared spectroscopy, along with DFT, we identified multiple magnetic phases with large unit cells, leading to distinct zone-folded phonon series. These results demonstrate the strong coupling between the nontrivial spin configurations found in bulk CrOCl and lattice vibrations, highlighting the role of magnetoelastic interactions in frustrated magnets. Our findings expand the understanding of 2D magnetism, particularly in materials where frustration leads to unconventional spin states. The observed magnetic hysteresis and field-induced transitions provide a pathway to controlling spin configurations through external stimuli. Beyond fundamental research, these insights have implications for next-generation technologies. The ability to manipulate spin configurations in van der Waals magnets could have a significant impact on data storage, enabling ultradense and energy-efficient memory devices. These results pave the way for future studies on spin–lattice coupling and quantum information processing, positioning frustrated magnets as key materials in advanced spin-based technologies.

## EXPERIMENTAL AND COMPUTATIONAL DETAILS

**Growth of Bulk CrOCl.** CrOCl was prepared by chemical vapor transport (CVT) in a quartz glass ampule using chromium oxide and chromium chloride. In the quartz ampule (40 × 200 mm) were placed anhydrous chromium(III) chloride (99.9%, Strem, USA) and chromium oxide (99.9%, Sigma-Aldrich, Czech Republic) in stochiometric ratio corresponding to 20 g of CrOCl together with 0.3 g of $HgCl_2$ (99.9%, Sigma-Aldrich, Czech Republic). The ampule was melt-sealed under high vacuum ($1 \times 10^{-3}$ Pa) by an oxygen–



https://doi.org/10.1021/acsnano.5c03174
ACS Nano 2025, 19, 23693–23702

hydrogen welding torch. The ampule was first prereacted in a crucible furnace by gradual heating up to 900 °C. Subsequently, the ampule was placed in a two-zone horizontal furnace. First, the source zone was heated at 800 °C, while the growth zone was heated at 950 °C. After 4 days, the thermal gradient was reversed, and the source zone was heated at 900 °C, and the growth zone at 850 °C. Over the period of 15 days, the temperature of the source zone was increased to 950 °C, and the growth zone temperature was decreased to 800 °C. Finally, the ampule was cooled down to room temperature and opened in an argon-filled glovebox.

**Magnetization Measurements.** Pulsed-field magnetization up to 60 T was measured at the Dresden High Magnetic Field Laboratory. The field was produced by a magnet solenoid energized by a single 1.44 MJ capacitor module. The rise time of the field pulse was 7 ms with a total pulse length of 25 ms. Magnetization was obtained by integrating the voltage induced in a compensated coil system surrounding the sample. A detailed description of the technique is provided in ref 39.

**Raman Scattering.** The magneto-Raman scattering response of bulk CrOCl was measured using a homemade experimental setup. The excitation laser is focused on the sample by a long working distance objective (12 mm), which is also used to collect scattered signals, which are sent using free beam optics to a grating spectrometer equipped with a liquid nitrogen-cooled CCD. Three volume Bragg filters are used in series before the spectrometer to remove the elastic scattering. This setup is then placed in a metallic tube filled with helium exchange gas and inserted into liquid helium. We use an optical power of 50 $\mu$W focused on ∼1 $\mu$m and a typical acquisition time for the Raman scattering response of 300 s.

**Infrared Measurements.** The infrared response has been measured using a Fourier transform spectrometer coupled to the resistive magnet with an oversized waveguide. The sample is placed in a closed tube filled with helium exchange gas, and the signal is collected by a composite silicon bolometer placed behind the sample. We use a rotating sample holder to change the in situ value between the sample and a reference to measure the absolute transmission of the sample. Static magnetic fields up to $B$ = 16 T have been produced by a superconducting solenoid.

**Magneto-Optical Kerr Effect Measurements.** Visible magneto-optical Kerr spectroscopy at 4 K was measured upon reflection in a polar configuration with a magnetic field applied perpendicular to the sample surface and nearly normal light incidence. We employed a custom-built magneto-optical spectrometer based on a rotating analyzer technique coupled to the Quantum Design Physical Property Measurement System. The applied magnetic field ranged from −6 to 6 T, and the measured spectral region covered energies from 1.2 to 4 eV.

**Computational Details.** Phonon calculations were performed using the finite displacements in the supercell method, as implemented in the Phonopy package.[40,41] The interatomic forces were extracted from DFT calculations using Quantum Espresso.[42,43] The Perdew−Burke−Ernzerhof (PBE)[44] version of generalized gradient approximation (GGA)[45] for the exchange−correlation functional has been used with a plane-wave basis set and norm-conserving pseudopotentials.[46,47] In this way, scalar-relativistic spin-polarization calculations were performed for every magnetic cell. Plane-wave kinetic energy cutoffs of 150 and 600 Ry were used for wave functions and the charge density, respectively. Because only the Γ-point of the Brillouin zone is of interest in optically excited phonons, and since Γ-point calculations are always "exact",[48] the magnetic primitive cell size was used as the smallest supercell size possible for lighter calculations.

Calculations were performed for three different magnetic structures. The FM phase (see Figure 1i) was calculated in the *Pmmn* cell (space group 59) with the room-temperature experimental[21] lattice constants $a$ = 3.863 Å, $b$ = 3.863 Å, and $c$ = 7.694 Å. In this phase, the Wyckoff positions are 2*a*, 2*b*, and 2*b* for the Cr, O, and Cl atoms, respectively. There are a total of six atoms in the unit cell. The AFM phase (see Figure 1e) was calculated in a 24-atom 1 × 4 × 1 cell, and the FiM phase (see Figure 1f) in a 30-atom 1 × 5 × 1 cell. The AFM cell has *P*21/*m* (space group 11) symmetry and the FiM cell has *Pmmn* (space group 59) symmetry.

Using the Monkhorst−Pack method,[49] the Brillouin zones corresponding to the FM, AFM, and FiM cells were sampled with 9 × 11 × 5, 9 × 3 × 5, and 9 × 2 × 5 k-point meshes, respectively, in accordance with cell size. Shifted k-meshes were used for relaxations only in order to reduce the number of treated k-points by symmetry. The nonshifted meshes containing the Γ-point were used for force calculations. Raman intensity calculations have been performed using the Phonopy Spectroscopy module.[50] This method recasts the Raman intensity tensors in terms of the macroscopic high-frequency dielectric tensor by using the central-difference scheme. Based on the equations,[50] it was found that the minimal precision to properly treat low-intensity modes required an accuracy on the computed static dielectric tensors of $10^{-4}$ au. Nonanalytical term corrections have been included in the phonon band structure calculations using the dipole−dipole interaction formalism.[51−53]

## ASSOCIATED CONTENT

### Supporting Information

The Supporting Information is available free of charge at https://pubs.acs.org/doi/10.1021/acsnano.5c03174.

Additional data and analysis; temperature dependence of the Raman modes; additional Raman scattering data concerning the AFM to spin flop to FiM transition; description of the effects of magnetoelastic coupling; comparison between Raman scattering and infrared experiments; description of MOKE spectroscopy; and description of the different phonon modes and of the relaxation of the magnetic phases (PDF)

## AUTHOR INFORMATION


### Corresponding Authors

**Andrés Saúl** − *Aix-Marseille Université, CNRS, CINaM, 13284 Marseille, France;* orcid.org/0000-0003-0540-703X; Email: andres.saul@cnrs.fr

**Clément Faugeras** − *LNCMI, UPR 3228, CNRS, EMFL, Université Grenoble Alpes, 38000 Grenoble, France;* orcid.org/0000-0002-9615-8739; Email: clement.faugeras@lncmi.cnrs.fr

### Authors

**Amit Pawbake** − *LNCMI, UPR 3228, CNRS, EMFL, Université Grenoble Alpes, 38000 Grenoble, France;* orcid.org/0000-0002-6345-489X

**Florian Petot** − *Aix-Marseille Université, CNRS, CINaM, 13284 Marseille, France;* orcid.org/0009-0002-4334-5431

**Florian Le Mardelé** − *LNCMI, UPR 3228, CNRS, EMFL, Université Grenoble Alpes, 38000 Grenoble, France*

**Tristan Riccardi** − *LNCMI, UPR 3228, CNRS, EMFL, Université Grenoble Alpes, 38000 Grenoble, France; Université Grenoble Alpes, CNRS, Grenoble INP, Institut NÉEL, 38000 Grenoble, France*

**Julien Lévêque** − *Aix-Marseille Université, CNRS, CINaM, 13284 Marseille, France;* orcid.org/0000-0002-5157-0236

**Benjamin A. Piot** − *LNCMI, UPR 3228, CNRS, EMFL, Université Grenoble Alpes, 38000 Grenoble, France;* orcid.org/0000-0003-4858-2452

**Milan Orlita** − *LNCMI, UPR 3228, CNRS, EMFL, Université Grenoble Alpes, 38000 Grenoble, France;* orcid.org/0000-0002-9633-507X




https://doi.org/10.1021/acsnano.5c03174
*ACS Nano* 2025, 19, 23693−23702

**Johann Coraux** − *Université Grenoble Alpes, CNRS, Grenoble INP, Institut NÉEL, 38000 Grenoble, France*
**Michal Hubert** − *Faculty of Mathematics and Physics, Institute of Physics, Charles University, 121 16 Prague 2, Czech Republic*
**Jan Dzian** − *LNCMI, UPR 3228, CNRS, EMFL, Université Grenoble Alpes, 38000 Grenoble, France; Faculty of Mathematics and Physics, Institute of Physics, Charles University, 121 16 Prague 2, Czech Republic*
**Martin Veis** − *Faculty of Mathematics and Physics, Institute of Physics, Charles University, 121 16 Prague 2, Czech Republic*
**Yurii Skourski** − *Hochfeld-Magnetlabor Dresden (HLD-EMFL), Helmholtz-Zentrum Dresden-Rossendorf, 01328 Dresden, Germany*
**Bing Wu** − *Department of Inorganic Chemistry, University of Chemistry and Technology Prague, 166 28 Prague 6, Czech Republic;* orcid.org/0000-0002-9637-6787
**Zdenek Sofer** − *Department of Inorganic Chemistry, University of Chemistry and Technology Prague, 166 28 Prague 6, Czech Republic;* orcid.org/0000-0002-1391-4448
**Benoît Grémaud** − *Aix-Marseille Université, Université de Toulon, CNRS, CPT, 13284 Marseille, France;* orcid.org/0000-0001-6404-3817

Complete contact information is available at:
https://pubs.acs.org/10.1021/acsnano.5c03174

### Author Contributions

○A.P. and F.P. contributed equally to this work.

### Notes

The authors declare no competing financial interest.

## ACKNOWLEDGMENTS

This work was partially supported by LNCMI and HLD-HZDR, members of the European Magnetic Field Laboratory (EMFL). This work was also partially supported by France 2030 government investment plan, managed by the French National Research Agency under Grant Reference PEPR SPIN-SPINMAT ANR-22-EXSP-0007, by ANR-23-QUAC-0004 and by CEFIPRA CSRP Project No. 7104-2. Z.S. and B.W. were supported by ERC-CZ program (project LL2101) from Ministry of Education Youth and Sports (MEYS) and by the project Advanced Functional Nanorobots (reg. No. CZ.02.1.01/0.0/0.0/15-003/0000444 financed by the ERDF).

## REFERENCES

(1) Zapf, V.; Jaime, M.; Batista, C. D. Bose−Einstein condensation in quantum magnets. *Rev. Mod. Phys.* **2014**, *86*, 563−614.
(2) Giamarchi, T.; Rüegg, C.; Tchernyshyov, O. Bose−Einstein condensation in magnetic insulators. *Nat. Phys.* **2008**, *4*, 198−204.
(3) Shiramura, W.; Takatsu, K.-i.; Kurniawan, B.; Tanaka, H.; Uekusa, H.; Ohashi, Y.; Takizawa, K.; Mitamura, H.; Goto, T. Magnetization Plateaus in NH 4CuCl 3. *J. Phys. Soc. Jpn.* **1998**, *67*, 1548−1551.
(4) Mitamura, H.; Sakakibara, T.; Nakamura, H.; Kimura, T.; Kindo, K. Multiferroicity on the Zigzag-Chain Antiferromagnet MnWO4 in High Magnetic Fields. *J. Phys. Soc. Jpn.* **2012**, *81*, No. 054705.
(5) Wosnitza, J.; Zvyagin, S. A.; Zherlitsyn, S. Frustrated magnets in high magnetic fields—selected examples. *Rep. Prog. Phys.* **2016**, *79*, No. 074504.
(6) Wulferding, D.; Choi, Y.; Do, S.-H.; Lee, C. H.; Lemmens, P.; Faugeras, C.; Gallais, Y.; Choi, K.-Y. Magnon bound states versus anyonic Majorana excitations in the Kitaev honeycomb magnet α-RuCl3. *Nat. Commun.* **2020**, *11*, 1603.
(7) Sahasrabudhe, A.; et al. High-field quantum disordered state in $\alpha-RuCl_3$: Spin flips, bound states, and multiparticle continuum. *Phys. Rev. B* **2020**, *101*, No. 140410.
(8) Thede, M.; Mannig, A.; Månsson, M.; Hüvonen, D.; Khasanov, R.; Morenzoni, E.; Zheludev, A. Pressure-Induced Quantum Critical and Multicritical Points in a Frustrated Spin Liquid. *Phys. Rev. Lett.* **2014**, *112*, No. 087204.
(9) Schaller, A. M.; Bykov, M.; Bykova, E.; Glazyrin, K.; Rekis, T.; van Smaalen, S. Pressure-dependent distortions in quasi-two-dimensional magnetic CrOCl at low temperatures. *Phys. Rev. B* **2023**, *108*, No. 104108.
(10) Huang, B.; Clark, G.; Navarro-Moratalla, E.; Klein, D. R.; Cheng, R.; Seyler, K. L.; Zhong, D.; Schmidgall, E.; McGuire, M. A.; Cobden, D. H.; Yao, W.; Xiao, D.; Jarillo-Herrero, P.; Xu, X. Layer-dependent ferromagnetism in a van der Waals crystal down to the monolayer limit. *Nature* **2017**, *546*, 270−273.
(11) Fei, Z.; Huang, B.; Malinowski, P.; Wang, W.; Song, T.; Sanchez, J.; Yao, W.; Xiao, D.; Zhu, X.; May, A. F.; Wu, W.; Cobden, D. H.; Chu, J. H.; Xu, X. Two-dimensional itinerant ferromagnetism in atomically thin Fe3GeTe2. *Nat. Mater.* **2018**, *17*, 778−782.
(12) Kurosawa, K.; Saito, S.; Yamaguchi, Y. Neutron Diffraction Study on MnPS3 and FePS3. *J. Phys. Soc. Jpn.* **1983**, *52*, 3919−3926.
(13) Le Flem, G.; Brec, R.; Ouvard, G.; Louisy, A.; Segransan, P. Magnetic interactions in the layer compounds MPX3 (M = Mn, Fe, Ni; X = S, Se). *J. Phys. Chem. Solids* **1982**, *43*, 455−461.
(14) Jiang, X.; Liu, Q.; Xing, J.; Liu, N.; Guo, Y.; Liu, Z.; Zhao, J. Recent progress on 2D magnets: Fundamental mechanism, structural design and modification. *Appl. Phys. Rev.* **2021**, *8*, No. 031305.
(15) Geim, A. K.; Grigorieva, I. V. Van der Waals heterostructures. *Nature* **2013**, *499*, 419−425.
(16) Zhong, D.; Seyler, K. L.; Linpeng, X.; Cheng, R.; Sivadas, N.; Huang, B.; Schmidgall, E.; Taniguchi, T.; Watanabe, K.; McGuire, M. A.; Yao, W.; Xiao, D.; Fu, K.-M. C.; Xu, X. Van der Waals engineering of ferromagnetic semiconductor heterostructures for spin and valleytronics. *Sci. Adv.* **2017**, *3*, No. e1603113.
(17) Ciorciaro, L.; Kroner, M.; Watanabe, K.; Taniguchi, T.; Imamoglu, A. Observation of Magnetic Proximity Effect Using Resonant Optical Spectroscopy of an Electrically Tunable $MoSe_2/CrBr_3$ Heterostructure. *Phys. Rev. Lett.* **2020**, *124*, No. 197401.
(18) Huang, B.; McGuire, M. A.; May, A. F.; Xiao, D.; Jarillo-Herrero, P.; Xu, X. Emergent phenomena and proximity effects in two-dimensional magnets and heterostructures. *Nat. Mater.* **2020**, *19*, 1276−1289.
(19) Sierra, J. F.; Fabian, J.; Kawakami, R. K.; Roche, S.; Valenzuela, S. O. Van der Waals heterostructures for spintronics and opto-spintronics. *Nat. Nanotechnol.* **2021**, *16*, 856−868.
(20) Forsberg, H.-E.; Songstad, J.; Viljanto, J.; Seppälä, P.; Theander, O.; Flood, H. On the Structure of CrOCl. *Acta Chem. Scand.* **1962**, *16*, 777.
(21) Christensen, A. N.; Johansson, T.; Quézel, S. Preparation and Magnetic Properties of CrOCl. *Acta Chem. Scand.* **1974**, *28a*, 1171−1174.
(22) Reuvekamp, P. G. Investigation into the magnetic and the structural properties of two low-dimensional antiferromagnets TiPO4 and CrOCl. PhD thesis, University of Stuttgart: Stuttgart, Germany, 2014.
(23) Angelkort, J.; Wölfel, A.; Schönleber, A.; van Smaalen, S.; Kremer, R. K. Observation of strong magnetoelastic coupling in a first-order phase transition of CrOCl. *Phys. Rev. B* **2009**, *80*, No. 144416.
(24) Radtke, G.; Saúl, A.; Dabkowska, H. a.; Luke, G. M.; Botton, G. A. Interplay between Structural, Electronic, and Magnetic Degrees of Freedom in $Sr_3Cr_2O_8$. *Phys. Rev. Lett.* **2010**, *105*, No. 036401.
(25) Saúl, A.; Radtke, G. Magnetic couplings in $CsV2O_5$: a new picture. *Phys. Rev. Lett.* **2011**, *106*, No. 177203.
(26) Okada, M.; Tanaka, H.; Kurita, N.; Johmoto, K.; Uekusa, H.; Miyake, A.; Tokunaga, M.; Nishimoto, S.; Nakamura, M.; Jaime, M.; Radtke, G.; Saúl, A. Quasi-two-dimensional Bose−Einstein con-

densation of spin triplets in the dimerized quantum magnet $Ba_2CuSi_2O_6$. *Phys. Rev. B* **2016**, *94*, No. 094421.
(27) Saúl, A.; Gauthier, N.; Askari, R. M.; Côté, M.; Maris, T.; Reber, C.; Lannes, A.; Luneau, D.; Nicklas, M.; Law, J. M.; Green, E. L.; Wosnitza, J.; Bianchi, A. D.; Feiguin, A. Unconventional field induced phases in a quantum magnet formed by free radical tetramers. *Phys. Rev. B* **2018**, *97*, No. 064414.
(28) Vaclavkova, D.; Delhomme, A.; Faugeras, C.; Potemski, M.; Bogucki, A.; Suffczyński, J.; Kossacki, P.; Wildes, A. R.; Grémaud, B.; Saúl, A. Magnetoelastic interaction in the two-dimensional magnetic material MnPS3 studied by first principles calculations and Raman experiments. *2D Materials* **2020**, *7*, No. 035030.
(29) Rocquefelte, X.; Herak, M.; Miyake, A.; Lafargue-Dit-Hauret, W.; Berger, H.; Tokunaga, M.; Saúl, A. Coherent description of the magnetic properties of $SeCuO_3$ versus temperature and magnetic field. *Phys. Rev. B* **2023**, *107*, No. 054407.
(30) Gu, P.; et al. Magnetic Phase Transitions and Magnetoelastic Coupling in a Two-Dimensional Stripy Antiferromagnet. *Nano Lett.* **2022**, *22*, 1233−1241.
(31) Zhang, M.; Hu, Q.; Huang, Y.; Hua, C.; Cheng, M.; Liu, Z.; Song, S.; Wang, F.; Lu, H.; He, P.; Cao, G.; Xu, Z.; Lu, Y.; Yang, J.; Zheng, Y. Spin-Lattice Coupled Metamagnetism in Frustrated van der Waals Magnet CrOCl. *Small* **2023**, *19*, No. 2300964.
(32) Das, B.; Ghosh, S.; Kundu, T.; Paramanik, R.; Maity, S.; Palit, M.; Das, S.; Kumar Hazra, P.; Maji, P.; Ghosh, A.; Datta, S. Metamagnetism and Magnetocaloric Properties in a van der Waals Antiferromagnet CrOCl. *Phys. Status Solidi B* **2022**, *260*, No. 2200422.
(33) Allen, P. B.; Berlijn, T.; Casavant, D. A.; Soler, J. M. Recovering hidden Bloch character: Unfolding electrons, phonons, and slabs. *Phys. Rev. B* **2013**, *87*, 239904.
(34) Zhang, T.; et al. Magnetism and Optical Anisotropy in van der Waals Antiferromagnetic Insulator CrOCl. *ACS Nano* **2019**, *13*, 11353−11362. PMID: 31525955
(35) Xu, F.; Li, H.; Wang, N.; Wang, W.; Xu, J.; Zhu, W.; Liu, Y.; Zhang, C.; Qu, Z.; Xue, F. Magnetic field induced transitions probed in CrOCl flakes using dynamic cantilever magnetometry. *J. Appl. Phys.* **2023**, *134*, 163904.
(36) Yang, H.; Liang, J.; Cui, Q. First-principles calculations for Dzyaloshinskii−Moriya interaction. *Nature Reviews Physics* **2023**, *5*, 43−61.
(37) Cui, Q.; Zhu, Y.; Jiang, J.; Cui, P.; Yang, H.; Chang, K.; Wang, K. Anatomy of Hidden Dzyaloshinskii−Moriya Interactions and Topological Spin Textures in Centrosymmetric Crystals. *Nano Lett.* **2024**, *24*, 7358−7365.
(38) Wilson, N. P.; Lee, K.; Cenker, J.; Xie, K.; Dismukes, A. H.; Telford, E. J.; Fonseca, J.; Sivakumar, S.; Dean, C.; Cao, T.; Roy, X.; Xu, X.; Zhu, X. Interlayer electronic coupling on demand in a 2D magnetic semiconductor. *Nat. Mater.* **2021**, *20*, 1657−1662.
(39) Skourski, Y.; Kuz'min, M. D.; Skokov, K. P.; Andreev, A. V.; Wosnitza, J. High-field magnetization of $Ho_2Fe_{17}$. *Phys. Rev. B* **2011**, *83*, No. 214420.
(40) Togo, A.; Chaput, L.; Tadano, T.; Tanaka, I. Implementation strategies in phonopy and phono3py. *J. Phys.: Condens. Matter* **2023**, *35*, 353001.
(41) Togo, A. First-principles Phonon Calculations with Phonopy and Phono3py. *J. Phys. Soc. Jpn.* **2023**, *92*, No. 012001.
(42) Giannozzi, P.; et al. QUANTUM ESPRESSO: a modular and open-source software project for quantum simulations of materials. *J. Phys.: Condens. Matter* **2009**, *21*, 395502.
(43) Giannozzi, P.; et al. Advanced capabilities for materials modelling with Quantum ESPRESSO. *J. Phys.: Condens. Matter* **2017**, *29*, 465901.
(44) Perdew, J. P.; Burke, K.; Ernzerhof, M. Generalized Gradient Approximation Made Simple. *Phys. Rev. Lett.* **1996**, *77*, 3865−3868.
(45) Perdew, J. P.; Burke, K.; Wang, Y. Generalized gradient approximation for the exchange-correlation hole of a many-electron system. *Phys. Rev. B* **1996**, *54*, 16533−16539.
(46) Hamann, D. R.; Schlüter, M.; Chiang, C. Norm-Conserving Pseudopotentials. *Phys. Rev. Lett.* **1979**, *43*, 1494−1497.
(47) Hamann, D. R. Optimized norm-conserving Vanderbilt pseudopotentials. *Phys. Rev. B* **2013**, *88*, No. 085117.
(48) Parlinski, K.; Li, Z. Q.; Kawazoe, Y. First-Principles Determination of the Soft Mode in Cubic $ZrO_2$. *Phys. Rev. Lett.* **1997**, *78*, 4063−4066.
(49) Monkhorst, H. J.; Pack, J. D. Special points for Brillouin-zone integrations. *Phys. Rev. B* **1976**, *13*, 5188−5192.
(50) Skelton, J. M.; Burton, L. A.; Jackson, A. J.; Oba, F.; Parker, S. C.; Walsh, A. Lattice dynamics of the tin sulphides $SnS_2$, SnS and $Sn_2S_3$: vibrational spectra and thermal transport. *Phys. Chem. Chem. Phys.* **2017**, *19*, 12452−12465.
(51) Pick, R. M.; Cohen, M. H.; Martin, R. M. Microscopic Theory of Force Constants in the Adiabatic Approximation. *Phys. Rev. B* **1970**, *1*, 910−920.
(52) Gonze, X.; Charlier, J.-C.; Allan, D.; Teter, M. Interatomic force constants from first principles: The case of $\alpha$-quartz. *Phys. Rev. B* **1994**, *50*, 13035−13038.
(53) Gonze, X.; Lee, C. Dynamical matrices, Born effective charges, dielectric permittivity tensors, and interatomic force constants from density-functional perturbation theory. *Phys. Rev. B* **1997**, *55*, 10355−10368.


https://doi.org/10.1021/acsnano.5c03174
*ACS Nano* 2025, 19, 23693−23702